A Jiang–Tadmor Scheme on Unstructured Triangulations

Ivan Christov, Bojan Popov

Department of Mathematics, Texas A&M University,
College Station, TX 77843-3368, USA

Abstract

Nonoscillatory central schemes are a class of Godunov-type (i.e., shock-capturing, finite volume) numerical methods for solving hyperbolic systems of conservation laws (e.g., the Euler equations of gas dynamics). Throughout the last decade, central (Godunov-type) schemes have gained popularity due to their simplicity and efficiency. In particular, the latter do not require the solution of a Riemann problem or a characteristic decomposition to compute the intercell flux.

One example of a 2D central Godunov-type scheme is that of Jiang and Tadmor [SIAM J. Sci. Comput. 19 (1998) 1892–1917]. Unfortunately, the latter scheme is constructed on a uniform Cartesian (tensor product) grid and uses a direction-by-direction reconstruction. Therefore, the JT scheme is not applicable to problems with complicated domain geometry, and may not be able to achieve the full second order of accuracy (in time and space) when the solution is not aligned with the coordinate directions.

In this paper, an extension of the JT scheme to unstructured triangular grids will be discussed. To this end, a new, "genuinely multidimensional," nonoscillatory reconstruction — the minimum-angle plane reconstruction (MAPR) — is discussed. The MAPR is based on the selection of an interpolation stencil yielding a linear reconstruction (of the solution from its cell averages) with minimal angle with respect to the horizontal. Furthermore, numerical results are presented for hyperbolic systems of conservation laws with convex and nonconvex flux functions. In particular, it will be shown that the MAPR is able to capture composite waves accurately.

Key words: hyperbolic systems of conservation laws, nonoscillatory central Godunov-type schemes, Euler equations, adaptive mesh refinement
PACS: 47.11.Df, 52.35.Tc

Email addresses: `christov@math.tamu.edu` (Ivan Christov),
`popov@math.tamu.edu` (Bojan Popov).

1 Introduction

The first second-order accurate non-oscillatory central Godunov-type scheme was introduced by Nessyahu and Tadmor [1], whose work generalized the first-order accurate *staggered* Lax–Friedrichs scheme. Over the last decade, there has been a significant amount of research on the topic. Some of the recent work on central schemes includes, but is not limited to, semi-discrete formulations, less dissipative central-upwind schemes and extensions to multiple spatial dimensions (see, e.g., Refs. [2,3,4,5,6,7] and those therein).

In this paper, we present an extension of the second-order accurate (in space and time) two-dimensional (2D) central scheme of Jiang and Tadmor, which is a 2D version of the Nessyahu–Tadmor scheme [1], to unstructured triangular meshes. The Jiang–Tadmore scheme has been further refined by Kurganov and Tadmor [3] (the so-called *modified central differencing* scheme) by using the maximal local speeds of propagation. The extension of the Kurganov–Tadmor scheme to unstructured triangulations by way of the approach proposed in this article is straight-forward.

In light of the work of Kurganov and Petrova [4], which extended the "state-of-the-art" semi-discrete central-upwind schemes [5] to triangular meshes, we must motivate the present work. Our goal is to build the simplest possible *fully*-discrete central scheme on (trully) unstructured triangulations. In doing so, we are also proposing a novel "genuinely-multidimensional" reconstruction and showing how adaptive, unstructured meshes can significantly improve the performance of such a scheme. In addition, it should be noted that our work differs fundamentally from that of Arminjon *et al.* [7], who proposed an extension of the Nessyahu–Tadmor scheme to 2D unstructured triangulations, because we propose a novel (and simpler) nonoscillatory reconstruction based on the adaptive choice of an interpolation stencil and a staggered grid that fits naturally into the hierarchy of central schemes [3,5,4].

Furthermore, we hope to employ the scheme presented herein in a predictor-corrector-type algorithm that couples the (explicit) Godunov approach to conservation laws with the novel (implicit) finite-elements approach of the L^1-minimzation method of Guermond and Popov [8,9]. In this vein, we also hope to show how many of the common tools (e.g., tessellation of arbitrary domains, error indicators and adaptive mesh refinement, etc) of finite element methods can be seamlessly incorporated into Godunov-type finite volume schemes.

This paper is organized as follows. In Sec. 1.1, the problem is stated and basic notation for the paper is set out. In Sec. 2, the numerical method is described, including the reconstruction, evolution and projection steps. Finally, in Sec. 3, several numerical examples, including scalar equations (with both convex and

non-convex fluxes) and the Euler system of gas dynamics, are presented and discussed.

1.1 Statement of the Problem and Notation

We consider the following initial-value problem for a 2D hyperbolic system of conservation laws:

$$\begin{cases} \boldsymbol{q}_t + \boldsymbol{f}(\boldsymbol{q})_x + \boldsymbol{g}(\boldsymbol{q})_y = 0, & (x,y,t) \in \Omega \times (0,T], \\ \boldsymbol{q}(x,y,t=0) = \boldsymbol{q}_0(x,y), & (x,y) \in \Omega, \end{cases} \tag{1}$$

where $\Omega \subset \mathbb{R}^2$ is the interior of a polygonal domain, whose boundary we denote by $\partial\Omega$. In addition, let $\mathcal{T}$ be a *conforming* triangulation (see, e.g., [10, p.56] of $\bar{\Omega} := \Omega \cup \partial\Omega$, i.e. a finite collection of, say, N subsets τ of $\bar{\Omega}$, called elements, each of which is a non-degenerate triangle (usually satisfying a minimum-angle condition). We denote by $|\tau|$ the area of an element $\tau \in \mathcal{T}$.

Furthermore, let $\boldsymbol{w}$ be the approximation to $\boldsymbol{q}$, the true solution to (1), on the triangulation $\mathcal{T}$. Then, the constant $\bar{\boldsymbol{w}}_i^n$ stands for the approximate average of the solution over the element $\tau_i \in \mathcal{T}$ at time $t = t^n$, i.e.

$$\bar{\boldsymbol{w}}_i^n \approx \bar{\boldsymbol{q}}_i^n := \frac{1}{|\tau_i|} \int_{\tau_i} \boldsymbol{q}(x,y,t^n) \, \mathrm{d}A, \tag{2}$$

where $\mathrm{d}A := \mathrm{d}x \, \mathrm{d}y$. Moreover, given a fixed time step Δt, we define $t^n := n\Delta t$.

Finally, throughout the text we represent points in Euclidean space by ordered pairs, e.g. (x,y). However, if an ordered pair is followed by a $\top$ superscript, e.g. $(\nu_x, \nu_y)^\top$, it stands for a (column) vector. In addition, a dot between two vectors denotes the usual Euclidean inner product.

2 Overview of the Scheme

2.1 Reconstruction

Without loss of generality, we restrict ourselves to the case of a scalar conservation law for the rest of this section. In the case of a system, the procedures described herein apply to each component of $\boldsymbol{w}$ (i.e., each equation) in the same manner — this is the so called componentwise approach to reconstruction and limiting.

Thus, to approximate (1), we begin each time step with a piecewise constant solution of the form

$$\bar{w}^n(x, y) = \sum_{i=1}^{N} \bar{w}_i^n \chi_i(x, y), \tag{3}$$

where χ_i is the characteristic function of the element τ_i — i.e., χ_i is unity for all $(x, y) \in \tau_i$ and zero everywhere else.

Then, we construct a piecewise polynomial interpolant of $\bar{w}^n(x, y)$:

$$w^n(x, y) = \sum_{i=1}^{N} p_i^n(x, y)\chi_i(x, y), \tag{4}$$

where p_i^n is a linear function in two variable. We require the reconstruction to be conservative, hence we must have that at the center of mass of the element τ_i, which we denote by (x_i^*, y_i^*), $w^n(x_i^*, y_i^*) \equiv p_i^n(x_i^*, y_i^*) = \bar{w}_i^n$. Consequently, the linear interpolant has the following explicit form:

$$p_i^n(x, y) = \bar{w}_i^n + \nabla p_i^n \cdot (x - x_i^*, y - y_i^*)^\top. \tag{5}$$

Clearly, the gradient ∇p_i^n uniquely determines each linear interpolant.

There has been a significant amount of work on how to choose ∇p_i^n on an unstructured mesh so that the piecewise-linear reconstruction (4) is nonoscillatory: slope-limited nearest-neighbor linear interpolation [11], slope-limited least-squares gradient recovery [7], "admissible" piecewise-linear reconstruction [4] (and the references therein), ENO reconstruction [12], WENO reconstruction [13], high-order logarithmic reconstructions [14] etc. We refer the reader to Refs. [15, pp.212–225] and [16, pp.31–41] for a comprehensive overview of nonoscillatory reconstruction on unstructured meshes. However, many of the proposed methods feature empirical parameters and ad-hoc assumptions, which we do not find robust. To this end, we propose the *minimum-angle plane reconstruction*, which is similar to the approach in [11], but also adds a bit of a ENO/UNO (see, e.g., [1,2,17]) flavor to the reconstruction.

Consider an element $\tau_i \in \mathcal{T}$ and its neighbors, which we define as the elements in $\mathcal{T}$ that share an edge with τ_i. For a triangulation of the type discussed in Sect. 1.1, τ_i may have either one, two or three neighbors, which we denote by τ_{i1}, τ_{i2} and τ_{i3} (see Fig. 1). There are two cases that require special attention. First, if τ_i has only two neighbors (i.e., one of τ_i's edges lies on $\partial\Omega$), then only one plane can be constructed and it is the minimum-angle plane. Second, if τ_i has only one neighbor (i.e., two of τ_i's edges lie on $\partial\Omega$) then its second and third neighbors are defined as the two neighbors of τ_i's first neighbor that are not τ_i itself.

Now, for the two cases when three neighbors of $\tau_i \in \mathcal{T}$ can be identified, we begin the minimum-angle plane reconstruction by calculating the four planes
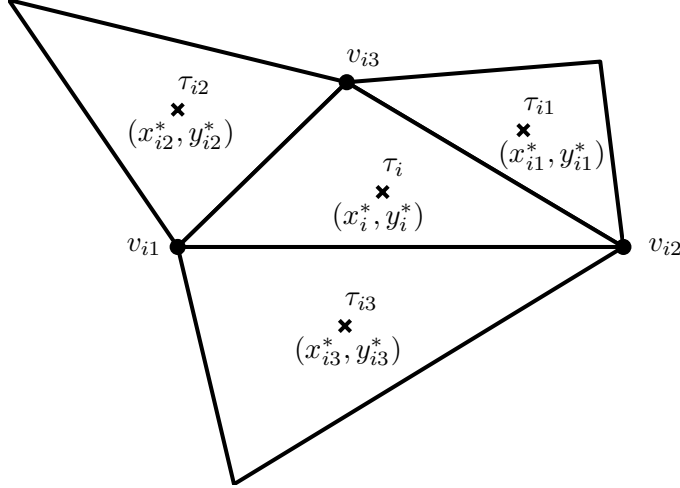
Fig. 1. Diagram of an element of the triangulation and its first neighbors.

that pass through the following collections of points:

(1) $(x_i^*, y_i^*, \bar{w}_i^n), (x_{i1}^*, y_{i1}^*, \bar{w}_{i1}^n), (x_{i2}^*, y_{i2}^*, \bar{w}_{i2}^n);$
(2) $(x_i^*, y_i^*, \bar{w}_i^n), (x_{i2}^*, y_{i2}^*, \bar{w}_{i2}^n), (x_{i3}^*, y_{i3}^*, \bar{w}_{i3}^n);$
(3) $(x_i^*, y_i^*, \bar{w}_i^n), (x_{i3}^*, y_{i3}^*, \bar{w}_{i3}^n), (x_{i1}^*, y_{i1}^*, \bar{w}_{i1}^n);$
(4) $(x_{i1}^*, y_{i1}^*, \bar{w}_{i1}^n), (x_{i2}^*, y_{i2}^*, \bar{w}_{i2}^n), (x_{i3}^*, y_{i3}^*, \bar{w}_{i3}^n).$

Then, we select the plane that concludes the smallest angle with the horizontal, where the angle is always corrected to the first quadrant.

Finally, let $\nu \equiv (\nu_x, \nu_y, \nu_z)^\top$ denote the normal vector to the minimum-angle plane over some $\tau_i \in \mathcal{T}$ at $t = t^n$, then it is easy to show that $\nabla p_i^n = -(\nu_x/\nu_z, \nu_y/\nu_z)^\top$. Thus, the piecewise-linear reconstruction (4) of the piecewise constant data (3) is complete.

2.1.1 Modifying the Reconstruction for Boundary Elements

Due to lack of information at the boundaries — boundary elements have only one or two neighbors — we add the boundary elements' *second neighbors* (i.e., their neighbors' neighbors) to the set of possible points through which the minimum-angle plane may pass. This results in stable interpolation at the boundaries, and does not degrade the solution. In fact, the second neighbors' may be used in for the selection of the minimum-angle plane for interior elements as well, if a more dissipative reconstruction is necessary for a certain problem.

5
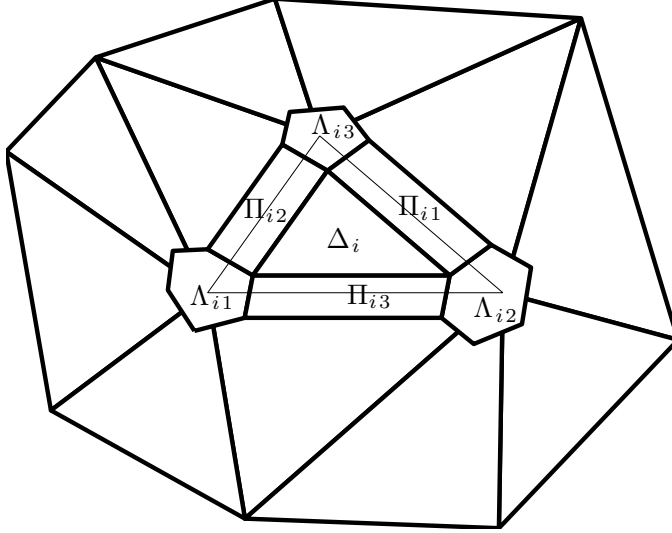
Fig. 2. Diagram of the staggered mesh superimposed onto the triangulation.

2.2 Evolution

In order to avoid solving Riemann problems at the interfaces of the elements in $\mathcal{T}$, we define a staggered mesh $\mathcal{S}$, whose elements contain the Riemann fans emanating from the discontinuities in the piecewise linear solution. Then, we realize the solution at the next time step by its averages over elements of $\mathcal{S}$.

To this end, assuming a suitable CFL condition holds, the discontinuity in w^n along the edges and at the vertices of each $\tau_i \in \mathcal{T}$ cannot propagate into the sub-triangle Δ_i, whose vertices are located at *one-third* of the distance from the vertices of τ_i to its center of mass (x_i^*, y_i^*). However, the discontinuities in w^n at every vertex do propagate into all elements of $\mathcal{T}$ that share it. Therefore, we define Λ_{ij} to be the polygonal domains about each vertex of τ_i, in which the piecewise linear interpolant (4) is discontinuous due to the jumps emanating from those edges (of τ_i and its neighbors) which share the vertex; $j \in \{1, 2, 3\}$ is an index over the vertices of τ_i. Furthermore, we denote by Π_{ij} the parallelograms which contain the discontinuities emanating from the edges of τ_i only; $j \in \{1, 2, 3\}$ is an index over the neighbors of τ_i. Fig. 2 illustrates the elements of the staggered mesh $\mathcal{S} = \cup_{i,j}\{\Delta_i, \Lambda_{ij}, \Pi_{ij}\}$ that overlap with some $\tau_i \in \mathcal{T}$.

Two remarks are in order here:

(1) If $|\Delta_i| = |\Pi_{ij}| \equiv 0$ ($\forall i, j$), the staggered grid becomes the well-known Voronoi diagram, which is commonly used in finite volume methods for elliptic problems (see Refs. [10, pp.262–265] and [16, pp.44–45]).
(2) If the maximum local speed of propagation is used to determine the vertices of Δ_i, we get the analogue of Kurganov and Tadmor's modified

central differencing [3] for (unstructured) triangulations.

Here, we should note that the CFL condition $\Delta t < \frac{1}{3} \cdot \min_i |\tau_i|/S_{\max}$, where $S_{\max}$ is the fastest wave's speed, ensures that all of the above assumptions are indeed true. However, in practice, $\Delta t < \frac{1}{3} \cdot \min_i \operatorname{diam}(\tau_i)/S_{\max}$ is sufficient to ensure stability. The latter CFL condition is the equivalent to the one used in [4].

Now, we evolve the piecewise linear function (4) according to the conservation law (1) over the *staggered* mesh $\mathcal{S}$ rather than the original triangulation $\mathcal{T}$. To this end, we require that the approximate solution $\boldsymbol{w}$ satisfy (1) subject to the initial condition $\boldsymbol{w}(x, y, t^n) = \boldsymbol{w}^n(x, y)$. We proceed by integrating the equation over $\sigma_k \times [t^n, t^{n+1}]$, where $\sigma_k \in \mathcal{S}$ is any one of the staggered elements described above. Then, after applying the fundamental theorem of calculus to the temporal integral of $\boldsymbol{w}_t$, we obtain that

$$\bar{\mathfrak{w}}_k^{n+1} = \bar{\mathfrak{w}}_k^n - \frac{1}{|\sigma_k|} \int_{t^n}^{t^{n+1}} \int_{\sigma_k} \boldsymbol{f}(\boldsymbol{w})_x + \boldsymbol{g}(\boldsymbol{w})_y \, \mathrm{d}A \, \mathrm{d}t, \qquad (6)$$

where $\bar{\mathfrak{w}}_k^{n+1}$ denotes the (staggered) average of w over σ_k at $t = t^{n+1}$. Moreover, it follows from the initial condition that

$$\bar{\mathfrak{w}}_k^n = \frac{1}{|\sigma_k|} \int_{\sigma_k} \boldsymbol{w}^n(x, y) \, \mathrm{d}A. \qquad (7)$$

Note that, since $\boldsymbol{w}^n$ is a piecewise linear function, the integral in (7) can be evaluated *exactly* by the midpoint quadrature rule, provided it is split up into a sum of integrals over parts of σ_k on which $\boldsymbol{w}^n$ is smooth.

We proceed by applying the divergence theorem to the spatial integral on the right-hand side of (6) to get

$$\bar{\mathfrak{w}}_k^{n+1} = \bar{\mathfrak{w}}_k^n - \frac{1}{|\sigma_k|} \int_{t^n}^{t^{n+1}} \oint_{\partial \sigma_k} \boldsymbol{f}(\boldsymbol{w})\nu_x + \boldsymbol{g}(\boldsymbol{w})\nu_y \, \mathrm{d}s \, \mathrm{d}t, \qquad (8)$$

where $\partial \sigma_k$ denotes the boundary of σ_k, $\nu \equiv (\nu_x, \nu_y)^\top$ denotes the outer normal vector to $\partial \sigma_k$ and $(\mathrm{d}s)^2 = (\mathrm{d}x)^2 + (\mathrm{d}y)^2$. Note that everything up to this point is *exact*.

We continue by employing the *midpoint* quadrature rule to approximate the temporal integral on the right-hand side of (8), admitting a $\mathcal{O}\!\left[(\Delta t)^2\right]$ local truncation error. Since we assumed the appropriate CFL condition holds so that the discontinuities in the solution do not leave the staggered mesh's elements during the current time step, the solution at $t = t^{n+\frac{1}{2}}$ is smooth along $\partial \sigma_k$, and so we are justified in using the midpoint rule, and we have formal

second-order accuracy in time. Consequently,

$$\bar{\mathfrak{w}}_k^{n+1} \approx \bar{\mathfrak{w}}_k^n - \frac{\Delta t}{|\sigma_k|} \oint_{\partial \sigma_k} \boldsymbol{f}\left(\boldsymbol{w}(x,y,t^{n+\frac{1}{2}})\right)\nu_x + \boldsymbol{g}\left(\boldsymbol{w}(x,y,t^{n+\frac{1}{2}})\right)\nu_y \,\mathrm{d}s, \quad (9)$$

where $t^{n+\frac{1}{2}} := \frac{1}{2}(t^n + t^{n+1}) \equiv \left(n + \frac{1}{2}\right)\Delta t$. Alternatively, one could use the improved (though still second order) quadrature rule presented in [18] for the temporal integral.

In the spirit of the Jiang–Tadmor predictor-corrector scheme, we proceed by predicting the temporal midvalues, i.e. $\boldsymbol{w}(x,y,t^{n+\frac{1}{2}})$, assuming the point (x,y) is located away from discontinuities, which is the case along $\partial \sigma_k$. To this end, we expand $\boldsymbol{w}$ in a Taylor series in time about $t = t^n$, neglecting all terms of $\mathcal{O}\left[(\Delta t)^2\right]$, then we use the conservation law (1) to replace $\boldsymbol{w}_t$ by a known quantity (see [2]), and we obtain that

$$\boldsymbol{w}(x,y,t^{n+1/2}) \approx \boldsymbol{w}^n(x,y) - \frac{\Delta t}{2}\left(\frac{\partial \boldsymbol{f}}{\partial \boldsymbol{q}}\left(\boldsymbol{w}^n(x,y)\right)\frac{\partial \boldsymbol{w}^n}{\partial x} + \frac{\partial \boldsymbol{g}}{\partial \boldsymbol{q}}\left(\boldsymbol{w}^n(x,y)\right)\frac{\partial \boldsymbol{w}^n}{\partial y}\right),$$
$$(10)$$

where $\partial \boldsymbol{f}/\partial \boldsymbol{q}$ and $\partial \boldsymbol{g}/\partial \boldsymbol{q}$ are the Jacobian matrices corresponding to the flux functions. In addition, the (limited) slopes $\partial \boldsymbol{w}^n/\partial y$ and $\partial \boldsymbol{w}^n/\partial x$ above must conditionally defined so that it takes the value of ∇p_i^n over the parts of $\sigma_k \in \mathcal{S}$ that overlap some $\tau_i \in \mathcal{T}$. Finally, we observe that (10) constitutes the predictor step, whereas (9) constitutes the corrector step of the scheme.

We conclude the derivation of the fully-discrete scheme by computing the boundary integral in (9) via the composite *trapezoidal* quadrature rule, since (by construction) $\partial \sigma_k$ is composed of a number of line segments whose endpoints are known (see Fig. 2). Consequently, the scheme is, formally, second-order accurate in space and (as already stated) in time.

Due to length considerations we omit the explicit calculation of each line integral in (9), and each double integral in (7), since they depend on the geometry of each of the three different types of elements of $\mathcal{S}$ (see Fig. 2). However, the calculations are straight-forward, though tedious.

2.3 Reconstruction on the Staggered Mesh

Given an element $\sigma_i \in \mathcal{S}$ and its neighbors σ_{ij}, $1 \leq j \leq m$, find all $\binom{m+1}{3}$ possible linear functions in two variable that pass through any triplet of 3D points in the collection, each of which is defined as the σ_i's (or σ_{ij}'s) center of mass and value of $\mathfrak{w}^n$ there. Then, retain the linear reconstruction that makes the smallest angle with the horizontal, and use it to find a *limited* gradient. In other words, the reconstruction step on the staggered mesh is conceptually

(and to a large extent practically) identical to the reconstruction step on the original triangulation.

2.4 Projection/Reaveraging

Finally, we complete each time step by computing the averages over the elements of the original triangulation $\mathcal{T}$ from the piecewise-linear reconstruction of the solution on the staggered mesh $\mathcal{S}$, i.e. $\forall \tau_i \in \mathcal{T}$

$$\bar{\boldsymbol{w}}_i^{n+1} = \frac{1}{|\tau_i|} \int_{\tau_i} \mathfrak{w}^{n+1}(x, y)\, \mathrm{d}A, \tag{11}$$

which can be evaluated exactly using the midpoint quadrature rule, provided it is split-up into integrals over the parts of domain on which the integrand is smooth [just like the integral in (7)], because $\mathfrak{w}^{n+1}$ is a piecewise linear function.

2.5 Implementation of Boundary Conditions

Following [12,15], we implement boundary conditions by modifying the flux integrals (9) directly when $\partial \sigma_k \cap \partial \Omega \neq \emptyset$ (i.e., when we are integrating along the boundary of the domain), rather than modifying the integrals indirectly by padding the computational domain with *ghost cells* as commonly done in the literature. Of course, if the mesh is to be truly unstructured, it is not clear whether the concept of a ghost cell (in the usual sense) is well-defined.

2.6 Adaptive Mesh Refinement and Refinement Indicators

Adaptive mesh refinement (AMR) can be incorporated seamlessly into our algorithm. For example, we could use a simple refinement indicator, such as those proposed in [15, pp.258–275], to refine and coarsen the mesh at each time step, depending on where the discontinuities in the solution propagate. As far as central schemes are concerned, an AMR algorithm for the case of a 2D triangular mesh and a dual mesh consisting of centroid-median cells (similar to the Voronoi diagram special case of our dual grid, see [16, pp.35–39]) was proposed in [19] and shows promise. In addition, the recent work [20] has shown how a central scheme with AMR can be implemented on non-matching (i.e., non-conforming) Cartesian grids in 3D. Finally, it must be noted that a more sophisticated, theoretically-motivated, smoothness indicator for conservation laws based on the so-called weak Lip'-norm, which can be used as a refinement indicator, was developed in [21].

Table 1
Error in the solution to (12) at $t = 0.5$ on a *structured*, uniform triangulation of Friedrichs–Keller type (see, e.g., [10]), as the mesh is refined.

h	L^∞ error	order	L^2 error	order	L^1 error	order
0.134321	0.140014	–	0.0665534	–	0.0512658	–
0.0671606	0.060454	1.21166	0.0229288	1.53735	0.0170446	1.58869
0.0335803	0.0238228	1.34349	0.00772257	1.57001	0.00536489	1.66769
0.0167902	0.00964388	1.30466	0.00251898	1.61625	0.00164701	1.70371
0.00839508	0.00388086	1.31323	0.000792697	1.66799	0.000471062	1.80585

3 Numerical Results

3.1 Constant-Coefficient Linear Advection

To show that the scheme presented in Sec. 2 is indeed second-order accurate in space and time, we solve the advection equation:

$$\begin{cases} u_t + u_x + u_y = 0, & (x, y, t) \in [0, 1]^2 \times (0, 0.5], \\ u(x, y, 0) = \sin[\pi(x + y)], & (x, y) \in [0, 1]^2, \end{cases} \tag{12}$$

subject *exact* boundary conditions (i.e., at an inflow boundary, the values of the conserved quantities are prescribed via the exact solution) on $\partial\Omega$, which has the exact solution $u(x, y, t) = \sin[\pi(x + y - 2t)]$.

The convergence results for this IBVP and estimated orders of accuracy are presented in Table 1. Though they are in exact agreement with those reported in [11], we do not seem to be able to achieve the full second-order accuracy in *both* the L^1 and L^∞ norms obtained in [4]. Note that h can be taken to be any measure of the "fineness" of the mesh as far as the experimental order of convergence is concerned, e.g. $h = \max_i \operatorname{diam}(\tau_i)$, where $\operatorname{diam}(\tau_i)$ is the largest side of the triangle τ_i. However, if we are to compare our results to those of schemes on rectangular meshes, we should take h to be the maximum radius of the circumscribed circles of the triangles of the meshes. The latter is the value given for h in Table 1. Finally, the CFL number used for these calculations was 1/5.
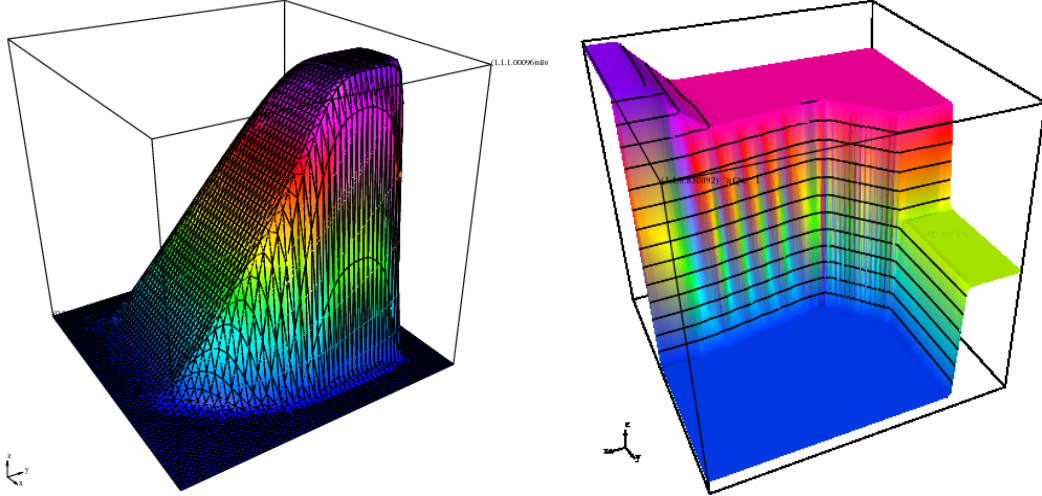
Fig. 3. (Left) 3D surface plot of the solution showing the mesh, which is a uniform Friedrichs–Keller triangulation with 6,272 elements, for the IC given by (14). (Right) 3D surface plot showing the solution contours for the IC given by (15) on a Friedrichs–Keller triangulation with 12,800 elements. The CFL number used was 1/5 in both cases.

3.2   Inviscid Burgers Equation

Next, we solve the following simple scalar equation considered in [2]:

$$u_t + \left(\tfrac{1}{2}u^2\right)_x + \left(\tfrac{1}{2}u^2\right)_y = 0, \quad (x,y) \in [0,1]^2, \tag{13}$$

subject to the "oblique" (Riemann problem) initial condition

$$u(x,y,0) = \begin{cases} -1.0, & x > 0,\ y > 0; \\ -0.2, & x < 0,\ y > 0; \\ 0.5, & x < 0,\ y < 0; \\ 0.8, & x > 0,\ y < 0. \end{cases} \tag{14}$$

and *exact* boundary conditions. The solution is advanced up to $t = 0.5$, in order to compare our results with those in [2].

In addition, we also consider (13) with the (Riemann problem) initial data

$$u(x,y,0) = \begin{cases} 1.0, & 0.1 \le x \le 0.6,\ 0.1 \le y \le 0.6; \\ 0.1, & \text{else.} \end{cases} \tag{15}$$

and Dirichlet boundary conditions on $\partial\Omega$. The solution is advanced up to $t = 0.3$, in order for the wavefront not to reach the boundary.

11
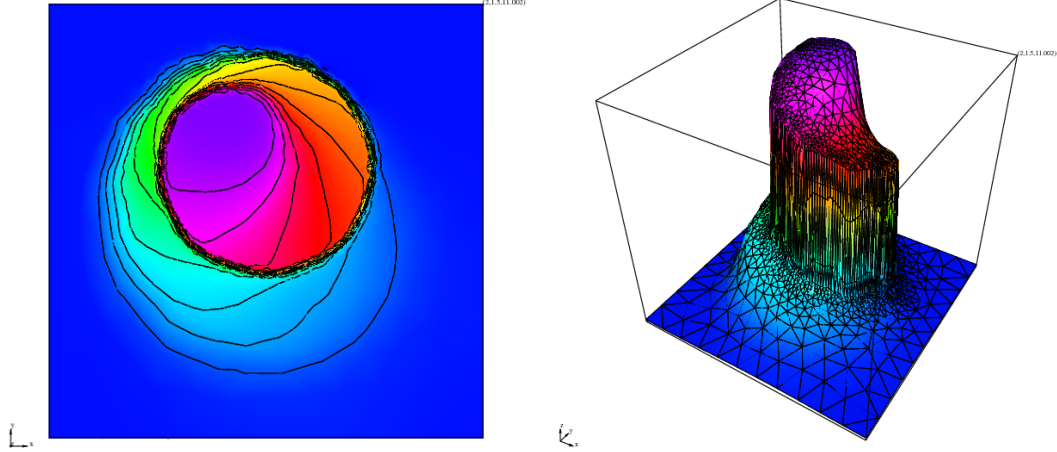
Fig. 4. (Left) 2D contour plot of the solution. (Right) 3D surface plot of the solution showing the (*a priori* refined) mesh with *only* 3,264 elements. The CFL number used was 1/6.

3.3   A Nonconvex, Nonlinear Equation

Finally, to demonstrate the robustness of the minimum-angle plane reconstruction, we consider an example proposed in [6], which results in the formation of a composite wave. The equation we wish to solve is the following scalar conservation law with a *nonconvex* flux (i.e., $f''(u)$ and/or $g''(u)$ may change sign):

$$u_t + (\sin u)_x + (\cos u)_y = 0, \quad (x, y, t) \in [0, 1]^2 \times (0, 1], \tag{16}$$

subject to the (Riemman problem) initial condition

$$u(x, y, 0) = \begin{cases} \dfrac{14\pi}{4}, & x^2 + y^2 < 1; \\ \dfrac{\pi}{4}, & \text{else.} \end{cases} \tag{17}$$

and natural (i.e., outflow) boundary conditions on $\partial\Omega$.

As the results in Fig. 4 show, the MAPR does not suffer from the problems pointed out in [6] that "less-dissipative" limiters (such as Superbee and WENO) do, for this nonconvex equation.

12

3.4 Euler Equations of Gas Dynamics

In two-dimensions, the governing equations for an ideal gas (i.e., the conservation of mass, momentum and energy) take the form

$$
\begin{pmatrix} \rho \\ \rho u \\ \rho v \\ E \end{pmatrix}_t + \begin{pmatrix} \rho u \\ \rho u^2 + p \\ \rho uv \\ u(E + p) \end{pmatrix}_x + \begin{pmatrix} \rho v \\ \rho uv \\ \rho v^2 + p \\ v(E + p) \end{pmatrix}_y = 0, \tag{18}
$$

where ρ is the density of the gas, p the pressure, u and v are the x- and y-velocities, respectively, and E is the total energy. The system is closed via the ideal gas equation of state:

$$
p = (\gamma - 1)\left[E - \frac{\rho}{2}(u^2 + v^2) \right]. \tag{19}
$$

First, we compare our solutions to the 4 state 2D Riemann problem to those computed by the central-upwind schemes on structured triangulations [4] and the various schemes on tensor product Cartesian grids (including JT) tested in [22]. Unfortunately, the 2D Riemann problem is, in some sense, an "artificial" scenario in as much as there are no physical boundary conditions one can impose. Therefore, we were forced to solve the problem, which is posed on $[0, 1]^2$, on $\Omega = [-0.5, 1.5]^2$ using a set of stable (tough incorrect) boundary conditions on $\partial\Omega$. In this manner, for the problems considered here, any (artificial) boundary effects do no propagate into $[0, 1]^2$ and so we can display the results in the latter domain with confidence. In Fig. 5 we present plots of two representative Riemann problems, which compare favorably with the results in [4,22,23].

Acknowledgments
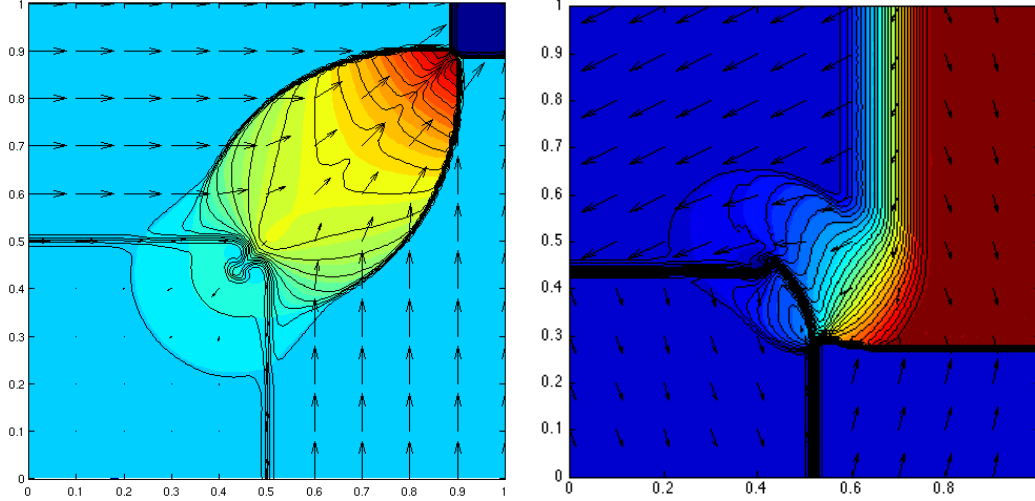
Fig. 5. Case 12 (left) and Case 15 (right) using the plotting convention of [22] — i.e., the black contours are of the density ρ, the color contours are of the pressure p and the arrows represent the velocity field $(u, v)^\top$. The mesh is a uniform Friedrichs–Keller triangulation with $\text{diam}(\tau_i) = \sqrt{2}/256$. The CFL number used was 0.275 in both cases.

References

[1] H. Nessyahu, E. Tadmor, Non-oscillatory central differencing for hyperbolic conservation laws, J. Comput. Phys. 87 (1990) 408–463.

[2] G.-S. Jiang, E. Tadmor, Nonoscillatory central schemes for multidimensional hyperbolic conservation laws, SIAM J. Sci. Comput. 19 (1998) 1892–1917.

[3] A. Kurganov, E. Tadmor, New high-resolution central schemes for nonlinear conservation laws and convection-diffusion equations, J. Comput. Phys. 160 (2000) 241–282.

[4] A. Kurganov, G. Petrova, Central-upwind schemes on triangular grids for hyperbolic systems of conservation laws, Numer. Methods Partial Differential Eq. 21 (2005) 536–552.

[5] A. Kurganov, S. Noelle, G. Petrova, Semidiscrete central-upwind schemes for hyperbolic conservation laws and Hamilton–Jacobi equations, SIAM J. Sci. Comput. 23 (2001) 707–740.

[6] A. Kurganov, G. Petrova, B. Popov, Adaptive semi-discrete central-upwind schemes for nonconvex hyperbolic conservation laws, SIAM J. Sci. Comput. (submitted).
URL `http://www.math.tamu.edu/~popov/KPP.pdf`

[7] P. Arminjon, M.-C. Viallon, A. Madrane, A finite volume extension of the Lax–Friedrichs and Nessyahu–Tadmor schemes for conservation laws on unstructured grids, Int. J. Comput. Fluid Dyn. 9 (1997) 1–22.

[8] J.-L. Guermond, A finite element technique for solving first-order PDEs in L^p, SIAM J. Numer. Anal. 42 (2004) 714–737.

[9] J.-L. Guermond, B. Popov, L^1-minimization methods for Hamilton–Jacobi equations: the one-dimensional case, Numer. Math. (submitted).
URL http://www.math.tamu.edu/~popov/HJ_1D.pdf

[10] P. Knabner, L. Angermann, Numerical methods for elliptic and parabolic partial differential equations, Vol. 44 of Texts in Applied Mathematics, Springer, 2003.

[11] L. J. Durlofsky, B. Engquist, S. Osher, Triangle based adaptive stencils for the solution of hyperbolic conservation laws, J. Comput. Phys. 98 (1992) 64–73.

[12] R. Abgrall, On essentially non-oscillatory schemes on unstructured meshes: analysis and implementation, J. Comput. Phys. 114 (1994) 45–58.

[13] C. Hu, C.-W. Shu, Weighted essentially non-oscillatory schemes on triangular meshes, J. Comput. Phys. 150 (1999) 97–127.

[14] R. Artebrant, Third order accurate non-polynomial reconstruction on rectangular and triangular meshes, J. Sci. Comput.
URL http://dx.doi.org/10.1007/s10915-005-9063-7

[15] D. Kröner, Numerical schemes for conservation laws, Wiley–Teubner, 1997.

[16] T. Barth, M. Ohlberger, Finite volume methods: foundation and analysis, in: E. Stein, R. de Borst, T. J. R. Hughes (Eds.), Encyclopedia of Computational Mechanics, Wiley, 2004.

[17] A. Harten, S. Osher, Uniformly high-order accurate nonoscillatory schemes. I, SIAM J. Numer. Anal. 24 (1987) 279–309.

[18] K.-A. Lie, S. Noelle, An improved quadrature rule for the flux-computation in staggered central difference schemes in multidimensions, J. Sci. Comput. 18 (2003) 69–81.

[19] M. Küther, M. Ohlberger, Adaptive second order central schemes on unstructured staggered grids, in: T. Y. Hou, E. Tadmor (Eds.), Hyperbolic Problems: Theory, Numerics, Applications, Springer, 2003, pp. 675–684.

[20] S. Noelle, W. Rosenbaum, M. Rumpf, 3D adaptive central schemes: Part I. Algorithms for assembling the dual mesh, Appl. Numer. Math. 56 (2006) 778–799.

[21] S. Karni, A. Kurganov, G. Petrova, A smoothness indicator for adaptive algorithms for hyperbolic systems, J. Comput. Phys. 178 (2002) 323–341.

[22] R. Liska, B. Wendroff, Comparison of several difference schemes on 1D and 2D test problems for the euler equations, SIAM J. Sci. Comput. 25 (2003) 995–1017.
URL http://www-troja.fjfi.cvut.cz/~liska/CompareEuler/compare8/

[23] A. Kurganov, E. Tadmor, Solution of two-dimensional Riemann problems for gas dynamics without Riemann problem solvers, Numer. Methods Partial Differential Eq. 18 (2002) 584–608.